DOI: https://doi.org/10.2138/am-2023-8978. http://www.minsocam.org/

Revision 1

Machine-learning oxybarometer developed using zircon trace-element chemistry and its applications

Shaohao Zou[1,*], Matthew J. Brzozowski[2], Xilian Chen[1], Deru Xu[1]

[1]State Key Laboratory of Nuclear Resources and Environment, East China University of Technology, Nanchang 330013, China

[2]Department of Geology, Lakehead University, Thunder Bay, Ontario P7B 5E1, Canada

*Corresponding authors: Shaohao Zou (shaohaozou@hotmail.com)

Deru Xu (xuderu@gig.ac.cn)

Abstract

Magmatic oxygen fugacity (fO_2) is a fundamental property to understanding the long-term evolution of the Earth's atmosphere and the formation of magmatic–hydrothermal mineral deposits. Classically, the magmatic fO_2 is estimated using the mineral chemistry, such as Fe–Ti oxides, zircon, and hornblende. These methods, however, are only valid within certain limits and/or requires a significant amount of a priori knowledge. In this contribution, a new oxybarometer, constructed by data-driven machine learning algorithm using the trace elements of zircons and their corresponding independent fO_2 constraints, is provided. Seven different algorithms are initially trained and then validated on a data set that was never utilized in the training processes. Results suggest that the oxybarometer constructed by the extremely randomized trees model has the best performance, with the largest R^2 value (0.91 ± 0.01), smallest RMSE (0.45± 0.03), and low propagated analytical error (~0.10 log units). Feature importance analysis demonstrates that U, Ti, Th, Ce, and Eu in zircon are the key trace elements that preserved fO_2 information. This newly developed oxybarometer has been applied in diverse systems, including the arc magmas and mid ocean ridge basalts, the fertile and barren porphyry systems, and the global S-type detrital zircon, which provide fO_2 constraints that are consistent with other independent methods, suggesting that it has wide applicability. To improve accessibility, the oxybarometer was developed into a software application aimed at enabling more consistent and reliable fO_2 determinations in magmatic systems, promoting further research.

Keywords: Machine learning; Zircon; Trace elements; Magmatic oxygen fugacity; Oxybarometer.

1. Introduction

Oxygen fugacity (fO_2) is a fundamental thermodynamic property governing the speciation and behavior of multivalent elements (e.g., S, Ce, Eu, Fe, and V) during magma evolution, which in turn controls their solubility, mobility, and compatibility in silicate magmas (Brounce et al. 2014; Ni et al. 2020). Estimates of fO_2 have been used to help address a range of important questions, including the compositional evolution of the atmosphere (Trail et al. 2011b; Lee and Bachmann 2014) and the mineralization potential of igneous rocks (Jugo et al. 2010; Sillitoe 2010; Richards 2015). Traditionally, the oxidation state of ancient rocks is constrained using the bulk-rock Fe^{2+}/Fe^{3+} ratio (Kress and Carmichael 1991; Brounce et al. 2014; Zhang et al. 2018), the Fe–Ti oxide oxybarometer (Ghiorso and Evans 2008), and the hornblende oxybarometer (Ridolfi and Renzulli 2012; Ridolfi 2021). Previous studies, however, have pointed out that these oxybarometers are only applicable in a limited range of conditions. For example, the bulk Fe^{2+}/Fe^{3+} ratio of a glass is easily reset by the subsequent metamorphism or alteration (Trail et al. 2011b), the Fe–Ti oxide oxybarometer is only applicable rapidly quenched volcanic rocks (Loucks et al. 2018), and the hornblende oxybarometer is only suitable for rocks emplaced deep in the crust because hornblende is unstable in the shallow crust (Rutherford and Hill 1993). Therefore, a more broadly applicable and robust oxybarometer is needed to unravel the complex interplay between fO_2, magmatic evolution, and metallogenesis through geological time.

Zircon is an ubiquitous accessory mineral in crustal rocks and is geochemically robustness, even in rocks that were hydrothermally altered, metamorphosed and weathered (Cherniak and Watson 2003; Trail et al. 2011a). Zircon contains a variety of trace elements, most of which include REEs, Ti, Y, U, Th, and Hf. These elements mainly enter into the zircon crystal lattice via isomorphic and coupled substitution mechanisms (Hoskin and Schaltegger 2003). The former includes $U^{4+} \leftrightarrow Zr^{4+}$, $Ti^{4+} \leftrightarrow Zr^{4+}$, $Hf^{4+} \leftrightarrow Zr^{4+}$, and $Ce^{4+} \leftrightarrow Zr^{4+}$, and the latter includes $(REEs + Y)^{3+} + Na^{+} / K^{+} / H^{+} \leftrightarrow Zr^{4+}$ and $P^{5+}/Nb^{5+} + (REEs + Y)^{3+} \leftrightarrow 2Zr^{4+}$. Substitution of these elements into zircon is related to the similarity of their ionic radius and charge to Zr^{4+}, which are controlled by the physicochemical conditions (e.g., temperature, oxidation state, and magma composition) of magma during mineral growth (Ballard et al. 2002; Ferry and Watson 2007). Oxidation state mainly affects substitution efficiency by changing the valence state of redox-sensitive elements. Consequently, the concentrations of the multivalent REEs (i.e., Ce and Eu) relative to the other monovalent REEs in zircon and the parent magma has become a popular proxy to characterize the fO_2 of magmas (Ballard et al. 2002; Trail et al. 2011b; Smythe and Brenan 2016; Loader et al. 2017; Zhong et al. 2019; Loucks et al. 2020). However, recent studies (Zhong et al. 2019; Zou et al. 2019) have demonstrated that such zircon REE oxybarometers may be unreliable given the difficulty of accurately determining the composition of the parent magma and the existence of REE-mineral inclusions within zircon. Accordingly, Loucks et al. (2020) proposed a new oxybarometer using ratios of Ce, U, and Ti in zircon (the U–Ti–Ce equation), which does not require knowledge of the parent magma composition. We have evaluated the reliability of the U–Ti–Ce equation of Loucks et al. (2020) by applying it to the global detrital zircon database from Tang et al. (2021) and reference therein. The results of this assessment demonstrate that some detrital zircons crystallized from a magma with an extremely (almost impossibly) reduced fO_2 (less than FMQ-5) (Fig. S1), indicating that the linearly regressed U–Ti–Ce equation does not capture all of the redox information of magmas and is not always valid. In addition, the U–Ti–Ce equation may not work well in the strongly peraluminous or peralkaline felsic magmas because their differentiation index (i.e., U/Ti) is not consistent with the variation of Ce/U ratio in melts (Loucks et al. 2020).

Recently, several studies have demonstrated that the data-driven machine learning methods can be powerful tools for solving complex problems in mineralogy, petrology, and geochemistry (Petrelli and Perugini 2016; Chen et al. 2021; Huang et al. 2022; Lin et al. 2022; Nathwani et al. 2022; Qin et al. 2022; Wang et al. 2022; Zou et al. 2022), and for the construction of thermobarometers (Petrelli et al. 2020; Higgins et al. 2022; Jorgenson et al. 2022; Li and Zhang 2022), without having any a priori knowledge. These research advances suggest that the machine learning method has the potential to be used for calibrating a mineral chemical-based oxybarometer. In this contribution, we present a novel machine learning-based approach to develop an oxybarometer using zircon trace-element chemistry and their corresponding fO_2 values obtained by other independent methods. Initially, seven different oxybarometers were first constructed and trained using prevalent machine learning algorithms, including linear regression, decision trees (Cramer et al. 1976), random forest (Breiman 2001), extremely randomized trees (ERT, Geurts et al. 2006), support vector machines (Smola and Schölkopf 2004), K nearest neighbors (Fukunaga and Narendra 1975) and XGboost (Chen and Guestrin 2016), and their performance was then benchmarked on a testing set to select an optimal algorithm. The calibrated oxybarometer was then applied in three different geological situations to test its performance and to explore the breadth of its applicability. To enhance accessibility, we developed a user-friendly web app and intuitive software with a graphical interface, which allow free online or offline fO_2 estimation from zircon chemistry using the machine learning oxybarometer, respectively. This study contributes a new tool to determine oxidation states in silicate melts without a priori knowledge. The approach circumvents limitations of existing methods dependent on specific equilibrium mineral pairs or intensive variables. With appropriate training data, it potentially provides a widely applicable oxybarometer to address outstanding questions on magma fO_2.

2. Data and methods

2.1. Data compilation and filtration

The data used to construct the machine learning models in this study were collated from published articles, and comprise zircon trace-element chemistry and independently constrained fO_2 values of their host rocks. The unfiltered calibration data set is composed of 1,450 data points of zircons from volcanic and plutonic rocks from 37 locations around the world; this data is summarized in Table S1 and the full data set can be found in Table S2. For the calibration of a robust oxybarometer, unreliable zircon analyses have been removed based on the following criteria. First, analyses with Th/U ratios less than 0.1 have been excluded to avoid metamorphic zircon (Kirkland et al. 2015). Second, analyses with La and P concentrations greater than 1 and 2000 ppm, respectively, have been removed as these analyses were likely contaminated by mineral inclusions (Zou et al. 2019; Zhu et al. 2020). Third, elemental data with >30% of the values as missing or 0 were not included. These criteria led to the selection of P, Ti, Y, Nb, Hf, Th, U, and other 14 REEs as the elements of interest and a dataset consisting of 1,369 zircon compositions with fO_2 values ranging from FMQ-4.9 to FMQ+2.75.

2.2. Data treatment of null values

Following the filtration, a log-transformation has been employed to the dataset, with the pre- and post-transformation features of the collected data illustrated in Figure S2. The purpose of this transformation is to ensure the distribution of elements approximate normality (Fig. S2b), thereby enhancing the performance of machine learning models, as disputed in previous studies (e.g., Frenzel et al. 2016; Petrelli et al. 2021). Regrettably, a significant amount (<30%) of the included elements contained null values or zeros, i.e., invalid data, which is an inevitability and may derived from different analytical procedures and instruments utilized to obtain the data. Consequently, the natural logarithm computation of null or 0 values becomes meaningless, producing misleading outcomes. To address this issue, various types of invalid data can be imputed using appropriate multiple strategies before applying the logarithmic transformation. In this study, the REEs are all analyzed in the collected data set, and the invalid values in the REEs data means they are below the detection limit; while invalid values in other elements indicate that they are not detected. Accordingly, we addressed this matter by employing the method proposed by van den Boogaart and Tolosana-Delgado (2013) to fill invalid data using normal distributions. For the REEs, the normal distribution was constructed with the mean and standard deviation parameters set to their respective detection limits, while for the other elements, the normal distribution was established based on the mean and standard deviation of not null data.

2.3. Dimensionality reduction

The correlation between the concentration of trace elements in zircon, especially the heavy REEs, is high (Fig. S3).If these highly correlated trace elements were to be utilized in the machine learning models, their interaction between elements would be masked and the noise information would be magnified, leading to overfitting and spurious interpretations (Hall 1999; Lösing and Ebbing 2021). To solve the problem that trace elements in zircon are highly correlated, the strategy of reducing data dimension and filtering noise by Principal Component Analysis (PCA) first, and then training the machine learning models was adopted in this study. The PCA method is a statistical procedure that identifies patterns among variables according to their correlations (Jackson 2005), and can map high-dimensional data to low-dimensional data while retaining as much information as possible from the original dataset (Abdi and Williams 2010). In addition, principal component loadings for each variable in the compositional biplots can provide the contribution of the variable to the principal component (Aitchison and Greenacre 2002), which can be used to discover the representative element associations.

2.4 Machine learning model

2.4.1. Data labeling

Supervised machine learning algorithms were adopted to calibrate the oxybarometer. Supervised machine learning is an algorithms that is trained by using labeled datasets to learn an appropriately function that maps the inputs (i.e., the trace-element composition of zircon in this study) to the predicted outputs (i.e., the fO_2 values in this study) using an the optimization algorithm (Chen et al. 2022). Once the training processes are complete, the trained model can be used as an oxybarmeter. Accordingly, the preparation of a dataset with calibrated labels is the key to constructing supervised machine learning models. In our case, the trace-element composition of zircon can be labeled using fO_2 values (expressed as ΔFMQ) obtained from the independent fO_2 constraints. Considering that the independent fO_2 constraints have some errors (Table S1), in this study, the trace-element composition of zircon from the same locality was labeled with random values from a normal distribution, and its mean and standard deviation are equal to the average fO_2 value and uncertainty in this area, respectively.

2.4.2. Machine learning model construction workflow

In this study, seven widely used supervised machine learning methods, including linear regression, decision trees (Cramer et al. 1976), random forest (Breiman 2001), extremely randomized trees (ERT, Geurts et al. 2006), support vector machines (Smola and Schölkopf 2004), K nearest neighbors (Fukunaga and Narendra 1975), and XGboost (Chen and Guestrin 2016), were used to calibrate the oxybarometer. Data processing and machine learning model construction procedures were completed in Python 3.10 utilizing the python packages, including Scikit-Learn (https://scikit-learn.org/stable/index.html) and XGboost (https://xgboost.readthedocs.io/en/latest/). A detailed description of the model building workflow used in this study (modified after (Li and Zhang 2022) and (Zou et al. 2021)) is illustrated in Fig. 1 and can be summarized in the following nine steps: (1) Data was collected from the pre-reviewed literatures and filtered based on the aforementioned criteria. (2) The collected data was preprocessed to meet the requirements of machine learning, including imputation of null data, log-transformation, data dimensionality reduction, and data labeling. (3) The filtered dataset was divided into a training (80% of the data) and testing (20% of the data) by stratified random splitting. The training set was used to train the model and optimize the hyperparameters, while the testing set was only used to evaluate the model. (4) A grid searching algorithm with 5-fold cross validation (CV) was used to select the optimal hyperparameters combination based on the performance metrics (i.e., coefficient of determination [R^2] score and root-mean-square error [RMSE]). Detailed regarding the tuning of hyperparameters can be found in Zou et al. (2022). (5) With the optimal hyperparameters combination, the training set was used to retrain the machine learning model, the performance of which was then evaluated using the testing set. (6) To avoid overfitting, the data preprocessing, random splitting, training, hyperparameters tuning, and model evaluation (i.e., steps 2, 3, 4 and 5) were repeated 1000 times, and 1000 paired R^2 scores and RMSE values were obtained. (7) By comparing the mean R^2 scores and RMSE values generated by different machine learning models, the best model (i.e., the one with the largest R^2 scores and the smallest RMSE values) was chosen as the target model. (8) The target model was then tuned using the entire filtered dataset using a grid searching algorithm with 5-fold CV to figure out the optimal hyperparameters combination. (9) The final, calibrated model was then trained using the entire dataset and the best hyperparameters combination obtained in step (8).

3. Results

3.1. Principal component analysis

PCA was performed on the entire filtered dataset to determine its dominant geochemical features. As illustrated in the compositional biplots, which combines the datapoints and PCA loadings (Figs. 2a and 2b), apart from a few abnormal data from the Lunar Highlands and kimberlites in southern Africa, most of the data are clustered together, and the 21 elements can be roughly be divided into three groups by the PC loadings — group 1 comprises U–Th–Ce, group 2 comprises of Ti, and group 3 comprises the REEs, with two subgroups for the light REEs and heavy REEs (Figs. 2a and 2b). The PCA loadings also confirm the strong correlation between the REEs (Figs. 2a and 2b). All of the elements, except for Ti, have negative loadings for the PC1. PC2 is mainly expressed by negative loadings for U, Th, and Ce and a positive loading for Ti. PC3 is dominated by a positive loading of La. The loadings for the other PCs can be found in the Figure S4. In the scree plot, the first seven PCs (from PC1 to PC7) cumulatively explain more than 90% of the total variance of the dataset (Fig. 2c), and the last nine PCs (from PC13 to PC21) cumulatively explain less than 1% of the variance (Fig. 2c). This means that PC1–PC7 preserve almost all the information of the original dataset. Accordingly, the noise in the entire dataset can be filtered out by reducing the dataset from its original 21 dimensions to 7 dimensions via the PCA method; we use these 7 dimensions to train our machine learning-based oxybarometer.

3.2. Comparation the performance of the different machine learning models

Previous studies have revealed that different machine learning algorithms exhibit unique strengths and weaknesses, with the most suitable model for a given task contingent on the data characteristics and intended outcomes (e.g.,Petrelli et al. 2020; Li and Zhang 2022). As a result, it is customary to leverage a range of diverse machine learning algorithms for specific tasks, followed by an assessment of each model's performance (quantifying the discrepancy between predicted and observed values) to identify the optimal algorithm. Typically, R^2 and RMSE values between predicted and observed values serve as evaluation metrics. A higher R^2 value implies a better model fit to true values, whereas a smaller RMSE value typically indicates reduced deviation between predicted and observed values. Consequently, both metrics are frequently employed to assess the performance of machine learning models. In this study, we apply this approach, where we computed the mean R^2 and RMSE values for 1000 repeated calculations using the identical dataset to assess and compare the performance of several machine learning models used to estimate fO_2. Figure 3 illustrates the probability density distributions of the R^2 and RMSE values for fO_2 estimations performed on the testing dataset.

Our results demonstrate that the performance of different machine learning models varies significantly, with R^2 values ranging from 0.3 to 0.9 and RMSE values ranging from 0.3 to1.25. Among all the models, the ERT algorithm exhibits the best performance, with the highest R^2 value of 0.91 ± 0.01 and the lowest RMSE value of 0.45 ± 0.03. In addition, the ERT model performs better than the previously proposed equation by Loucks et al. (2020), with higher R^2 and lower RMSE value during the 1000 times repeated calculations.

The ERT algorithm is a powerful machine learning technique that constructs an ensemble of decision trees and aggregates their predictions to make a final prediction. Previous studies have demonstrated that the ERT algorithm performs well on high-dimensional datasets with noisy features, due to its ability to reduce the impact of noisy features and avoid overfitting (Petrelli et al. 2020). Therefore, an ERT-based model was chosen to construct the final, calibrated machine learning-based oxybarometer in this study.

3.3. Estimation of error

The accuracy, stability, and uncertainty of the calibrated machine learning model must be assessed before it can be used as a reliable oxybarometer. During training and evaluation of the models, the probability density distributions of the R^2 and RMSE values of the extremely randomized trees model had the highest peaks and most constrained ranges, indicating that the model has limited variance and high stability (Fig. 3). The cross-validation error of the model can be expressed as RMSE of 0.45 ± 0.03.

The propagated error of the analysis uncertainties should also be evaluated; this can be estimated using the residual values (i.e., the difference between the measured fO_2 values and the predicted values from our model, (Jorgenson et al. 2022)). To avoid self-validation and overfitting, the uncertainties should be evaluated using data that was never used in the training process. Considering that the final constructed model was trained using the entire dataset, we performed a bootstrap resampling (n = 1000) Monte Carlo calculation (Keller and Schoene 2012) using zircon data with analytical errors equivalent to that of sample HB-18 (ΔFMQ = + 1.24) from (Meng et al. 2021) to generate new data that can maximally represent HB-18. As shown in Table S3, none of the newly generated zircon compositions appear in the training dataset. Thus, we used these new data to predict their fO_2 values using the calibrated machine learning-based oxybarometer; the predicted results and residuals are illustrated in Figure 4. The results demonstrate that the predicted mean fO_2 value (ΔFMQ = +1.39 ± 0.27) is slightly higher than the measured value (ΔFMQ = +1.24), but consistent with the measured value within the 1 sigma standard error estimate (SEE). As shown in Figure 4a, about 70% of predictions fall within the ±1 SEE range and the median residual of the 1000 values is 0.10 (Fig. 4b), suggesting that the analytical propagated error is about 0.10 log units, which is negligible relative to the model error (0.45 ± 0.03). For comparison, the equation from Loucks et al. (2020) was also used to predict the fO_2 values of the new data. Figure 4c and 4d demonstrates that this oxybarometer gives a predicted mean fO_2 value of 1.86 ± 0.72, with an analytical propagated error of 0.46 log units. This comparison reveals that the machine learning-based oxybarometer performs better under these conditions.

4. Discussion

4.1. Mapping relationships between trace elements in zircon and oxygen fugacity

In order to understand the relationship between zircon trace elements and their oxygen fugacity in machine learning model, it is imperative to discern the pivotal input data that governs the model's predictions. The Shapley Additive exPlanations

(SHAP), a game theory-based approach that indicates the output of machine learning models, is a widely recognized technique. It facilitates the interpretation of results by recognizing the contribution of each feature to the model's output. By utilizing the SHAP method, we can gain a better comprehension of how the model arrived at its predictions and identify the features (i.e., elements in this study) that significantly influence the model's prediction-making.

In this study, the SHAP method was used to help explain the relative importance of each PC to the output of the model; this was completed using the python package of SHAP (https://shap.readthedocs.io/en/latest/index.html). This method involves calculating the SHAP value for each feature (i.e., the PC in this study) of the sample, which represents the influence of that feature on the prediction (Lundberg and Lee 2017). A higher average absolute-size SHAP values for a feature indicates a higher influence on the prediction and vice versa. In addition, positive or negative SHAP values of each datapoint represents whether its output is positive or negative. Figure 5 shows the relative importance of features (i.e., the 7-diminational data) are ordered based on their mean absolute-size SHAP value. As shown in Figure 5a, relative importance scores, from high to low, are PC2, PC4, PC3, PC5, PC7, PC6, and PC1. Figure 5b shows the SHAP value of features for all individual analysis and also shows that how the high and low SHAP values of the features (i.e., PC1 to PC7) impact the model output. As shown in Figure 5b, the high values of PC2 and PC4 have the greatest contribution for the model to obtain negative values, whereas the low values of PC2 and PC4, and high values of PC5 have the greatest contribution to obtain positive values. These results reveal that PC2, PC4, and high values of PC5 significantly impact the model output. It is worth noting that PC2 always contributes more than the other PCs on the model output.

The features (i.e., PC1 to PC7) fed into the machine learning model are derived from the first seven principal components that cumulatively explain 90% of the variance of the original dataset. The PCA-derived loadings of elements can help characterize the relationships between the PC values and the elemental concentrations. Figure 2a and 2b illustrate that the low PC2 values are related to U–Th–Ce and its high values are related to Ti. Similarly, low PC4 values are mainly related to Eu and its high values are related to La (Fig. S4). High values of PC3 and PC5 are mainly derived from La and Eu, respectively (Fig. S4). Given that the La content of zircon is typically very low to the point that it is typically hard to measure accurately (Zhong et al. 2019; Zou et al. 2019) and the fact that La is missing in nearly 20% of the original dataset, the importance of La is likely being magnified, but the impact is still limited relative to other elements (i.e., U, Ti, Th, Ce, and Eu) used in the model because PC2 always contributes more than the other PCs. Accordingly, we can conclude that the U, Ti, Th, Ce, and Eu are the most important elements for the machine learning model and preserved fO_2 information.

Loucks et al. (2020) discussed, in detail, the relationships between the U, Ti, and Ce contents of zircons and the fO_2 conditions of their formation; this relationship was described using the equation of log $fO_2(\Delta FMQ) = 3.998(\pm 0.124) \times \log [Ce/\sqrt{(U_{initial} \times Ti)}] + 2.284\ (\pm 0.101)$ (i.e., the U–Ti–Ce equation). Along with the elements used in this equation, our machine learning model demonstrates that Th and Eu also preserve fO_2 information and are important to predicting fO_2 of a magma. This may be one of the reasons for the comparatively larger error of the fO_2 estimates using the above equation. Previous studies have demonstrated that the compatibility Th and Eu entering into zircon is controlled by oxygen fugacity (Burnham and Berry 2012). Because uranium is a redox-sensitive element with two major valance states (U^{4+} and U^{6+}), with U^{4+} being more compatible into zircon substitution of Zr^{4+}. Thorium in the tetravalent state behaves geochemically similar to U^{4+} because of their similar ionic radius, which may cause Th^{4+} and U^{4+} to compete for the Zr^{4+} position in zircon. Therefore, the Th/U ratio of zircon may be controlled by the environmental oxidation state of the magma. Similarly, Eu is also a redox-sensitive element and can exist as Eu^{3+} and Eu^{2+}. Eu^{3+} is more compatible into zircon than Eu^{2+}, and so a Eu anomaly in zircon can be used to estimate prevailing oxygen fugacity during its formation (Burnham and Berry 2012; Loader et al. 2017). Taken together, we can conclude that our constructed machine learning model correctly captures the relationship between trace elements in zircon and oxygen fugacity.

4.2. Applications of the machine learning-based oxybarometer to natural systems

To further explore the range of applicability of this machine learning-based oxybarometer, we have applied it to three different geological scenarios in which the

fO_2 has been well constrained by previous studies — i) arc magmas and mid ocean ridge basalts (MORB), ii) fertile and barren porphyry systems, and iii) a global database of S-type detrital zircon.

4.2.1. Estimation of fO_2 of arc magmas and MORB

Arcs and the mid ocean ridge are the two most important tectonic settings for the production of magmas globally, the former of which producing more oxidized magmas, on average, than the latter (Christie et al. 1986; Carmichael 1991; Brounce et al. 2014; Wang et al. 2019). Evidence from whole-rock Fe^{3+}/Fe^{2+}, V/Sc, and Zn/Fe_T ratios (Carmichael 1991; Lee et al. 2010; Brounce et al. 2014), Eu anomalies in zircon (Burnham and Berry 2012), and the composition of spinel and olivine (Evans et al. 2012; Wang et al. 2019) indicate that the measured fO_2 value at different times in most arc magmas vary from $\Delta FMQ = +0.5$ to +2 (locally up to +3), while MORBs have fO_2 values in the range of $\Delta FMQ = -1$ to +0.5 (Jugo et al. 2010; Evans et al. 2012; Richards 2015; Wang et al. 2019).

In this study, the composition of zircons from arcs and MORBs were used to validate the machine learning-based oxybarometer. Data for arcs (the Alenutian Arc, Andean Arc, and Central American Arc) were collated from the GEOROC database (https://georoc.eu/georoc/new-start.asp, accessed on October, 2022), and data for the Vema MORB are collected from (De Hoog et al. 2014); these data were filtered using criteria described above and are presented in Table S4. As illustrated in Fig. 6, the predicted mean fO_2 values of arcs are consistent with each other and are greater than that of the Vema MORB by approximately 1 log unit. In addition, the average fO_2 values for arcs range from 1.05 to 1.17 log units above the FMQ buffer (FMQ+1.05 to FMQ+1.17), whereas the average fO_2 value of the Vema MORB is similar to the FMQ buffer (FMQ-0.01). These results are in excellently agreement with the fO_2 constraints from previous works (Ballhaus 1993; Zhang et al. 2018). It is crucial to recognize that the most fO_2 proxies from previous studies on arc magmas and MORB most likely represent various stages of magma system evolution. Zircons are particularly effective at capturing fO_2 information from the more evolved intermediate to felsic magma products, whereas other proxies may be more sensitive to earlier, more mafic conditions. From this point, our machine learning-based oxybarometer, when combined with other proxies, has the potential to offer valuable insights into the changes in redox conditions experienced by arc magmas and MORB during their evolution.

4.2.2. Fertile and barren porphyry systems

Porphyry deposits are thought to form as a result of fluid exsolution derived from hydrous, volatile-rich and oxidized magmas (Sillitoe 2010; Richards 2015). It has been well established that, in oxidized magmas, S occurs as sulfate; in such environments, the sulfur content at sulfur saturation is higher, leading the presence of S undersaturated magmas that can interact with wall-rocks to form porphyry deposits (Streck and Dilles 1998; Jugo et al. 2010; Sillitoe 2010; Richards 2015; Shen et al. 2015; Sun et al. 2015). Therefore, the redox state of an intrusion is considered to have a significant impact on the formation of porphyry deposits, and has been used as one of the most important indicators to evaluate mineralization potential (Shen et al. 2015; Lu et al. 2016). Previous studies have demonstrated that the fertile rocks generally crystallized from highly oxidized (ΔFMQ > + 1) and hydrous magmas, whereas barren rocks generally crystallize from the relatively reduced (ΔFMQ < + 1) and dry melts (Richards 2015; Rezeau and Jagoutz 2020). Given the apparent link between fO_2 and mineralization potential, we also applied our machine learning-based oxybarometer to a large database of fertile and barren rocks from (Zou et al. 2022). Our calculation revealed the average fO_2 value of fertile rocks in this database is approximately 0.4 log units higher than that of barren rocks (FMQ + 1.40 vs. FMQ +0.62), with about 30% of data overlapping each other (Fig. 7). The overlap between the two rock groups may be attributed to the fact that the formation of porphyry deposits is not independently dictated by oxygen fugacity, but is also related to the water and volatile contents of the magma. It is, therefore, difficult to distinguish between fertile and barren rocks based solely on their fO_2 (Zou et al. 2022). Although overlap does exist, these results are consistent with others that fertile rocks generally form from higher fO_2 magmas than barren rocks.

4.2.3. Global S-type detrital zircons

The rise of atmospheric oxygen has had a profound impact on the chemical environment of the Earth's surface, ultimately leading to the evolution of a diverse biosphere (Kaufman et al. 2007; Lyons et al. 2014). It is widely agreed upon that two events caused the oxygen content of the atmosphere to rise to current levels: the Great Oxidation Event (GOE) that occurred approximately 2.5–2.2 billion years ago, and the later Neoproterozoic Oxidation Event (NOE) that occurred around 800–540 Myr ago (Bekker et al. 2004; Frei et al. 2009; Crowe et al. 2013; Planavsky et al. 2014; Liu et al. 2019; Chen et al. 2022; Hodgskiss and Sperling 2022). This established knowledge provides a basis for testing our oxybarometer. In this study, the detrital zircon derived from S-type granite (referred to as "S-type zircon") is employed to reconstruct the history of atmospheric oxygenation. S-type granites crystallize from strongly peraluminous magmas derived (dominantly) from metasedimentary rocks (Chappell and White 1992), which are derived from sedimentary rocks through several steps, including metamorphism, partial melting, and subsequent crystallization. As sediments provide a record of Earth surface processes, including variations in atmospheric oxygen levels, and are the precursors to S-type granites, it is reasonable to assume that the latter would also retain a record of atmospheric oxygen changes.

Trace element concentrations in zircon have been employed to distinguish S type zircon from others. One method for distinguishing S-type zircon involves examining its phosphorus concentration (e.g., Burnham and Berry 2017; Zhu et al. 2020). This method assumes that the higher solubility of apatite in peraluminous S-type granite magma results a relatively high phosphorus content in S-type zircon, assuming consistent zircon-melt P partition coefficients across diverse melts. However, recent study has shown that the reliability of this approach is limited to zircon samples younger than 720 Ma (Bucholz 2022; Bucholz et al. 2022), as the phosphorus content in S-type granite before this age does not consistently exceed that of other granites (Bucholz et al. 2022). As an alternative method, a machine learning approach utilizing trace element data from known zircon type has been proposed by Zhong et al. (2023). This method considers the influence of trace elements and has demonstrated high identification accuracy (about 0.85). It is important to note, however, that this approach did not incorporate ancient zircon samples predating 800 Ma in the model training process and, as a result, may not be suitable for analyzing zircon from these ages.

Therefore, this study aims to investigate the NOE through the fO_2 value of the global S-type detrital zircon with an age younger than 720 Ma. To achieve this goal, the trace-element composition of detrital zircons globally were collected from Tang et al. (2021) and references therein, and S-type zircons (< 720 Ma) were identified based on the criteria of Zhu et al. (2020): S-type zircons have a the molar concentration of REE +Y greater than 0.77 * P and less than 1.23 * P, and the molar concentration of P is greater than 15 μmol/g. After data filtering, a total of 116 data points of S-type detrital zircon were recognized, as shown in Table S5, and their fO_2 of formation was estimated using our machine learning-based oxybarometer. The predicted fO_2 values of S-type zircon is displayed in Figure 8, with a curve fit in every 100 Myr interval. Our findings are consistent with prior studies on sediments (e.g., Partin et al. 2013; Reinhard and Planavsky 2022), verifying a gradual increase in the fO_2 value of S-type detrital zircon from 800 Ma to 200 Ma (Fig. 8). Notably, our analysis reveals a distinctive shift in fO_2 levels of S-type zircons during the late Neoproterozoic period (650 Ma) (Canfield et al. 2007), coinciding with the timing of the NOE; and the sharp increase from 550–450 Ma, which is consistent with independent evidence indicating comprehensive ocean oxidation during that time (Fig.8b-c). Accordingly, although S-type zircon collected in this study do not provide a complete and continuous record of fO_2 fluctuations (Fig. 8), our study identifies key oxidation events. This highlights the effectiveness of the machine learning-based oxybarometer we developed, even in in strongly peraluminous environments.

4.3. Implications and possible uncertainty

Compared to the traditional oxybarometer, the data-driven machine learning oxybarometer in this study is constructed based on the contents of P, Ti, Y, Nb, Hf, Th, U and other 14 REEs in zircon. The greater number of elements used in the calibration process means that less meaningful information is lost, leading to higher precision and accuracy. More importantly, the successful application of the oxybarometer to the three different geologic systems (i.e., MORB–arc, porphyry systems, detrital zircons) suggests that it has the potential to be more widely applicable than traditional equations. The calibration approach does not require any a priori knowledge of physicochemical information and magma composition, which makes it a valuable tool for researchers studying a wide range of environments. However, further investigations with extensive datasets and analysis are needed to confirm the effectiveness of this approach for more different geological environments. For example, researchers could refine calibration procedures or develop new methods for predicting oxygen fugacity by collecting additional data (especially data with low fO_2 values that were not included in this study) and improving the existing model. The continuous development of this model could help researchers to understand the changes of fO_2 more accurately in diverse magma systems, which is essential for improving our understanding of crustal evolution.

The uncertainties of the machine learning model are significantly dependent on the features used. In this study, the input features are trace elements in zircon and the output feature is their corresponding fO_2 values. The bootstrap resampling Monte Carlo calculation shows that uncertainties from the analytical error of the input features is low (~0.01 log unit), which can largely be ignored compared to the model error. In contrast, the uncertainty of the output feature is more significant because of its relatively narrow range of possible values (between FMQ–4.9 and FMQ+3.0). The uncertainty in the output feature mainly comes from the fact that data with fO_2 values outside of this range have not been published so far, which leads to those data not being learned by the computer. Nevertheless, considering that the fO_2 of most natural magma systems is between FMQ–4.9 and FMQ+3 (Loucks et al. 2020), our model can still solve most problems. In addition, as more published data becomes available, the machine learning model will become increasingly more intelligent, and its performance will continuously improve. Lastly, when inputting the trace-element data into the model, we recommend using the average composition of several analyses on zircon from the same sample to avoid errors from spurious analyses.

4.4. Online web application and offline software

To make the oxybarometer more accessible and user friendly, a browser-based application and a GUI software (named ZirconfO2) have been developed, which can be used online (https://shaohaozou-fo2-webapp-7xqvo0.streamlit.app/) or offline (on Windows), respectively. These applications have been published on the GitHub platform (https://github.com/shaohaozou/fO2) and will be updated as additional geochemical data of zircon becomes publicly available.

The web-based oxybarometer and the GUI software are easy to use and do not need any programming knowledge. It should be noted that accessing the web-based oxybarometer requires a Streamlit account. Following the introduction provided on the webpage or within the software, users can upload their data in the same format as the template file (this can be download from the website) and click the “Calculate” and “Download your results” buttons in turn to complete the calculation and get the results.

5. Conclusions

We calibrated a new oxybarometer based on data-driven machine learning algorithms using the trace-element contents of zircon and their corresponding fO_2 constraints as model inputs. Although the developed oxybarometer does not provide a specific mathematical equation to illustrate the relationship between the trace-element content of zircon and oxygen fugacity, a reliable machine learning-based relationship has been recognized. In addition, this oxybarometer does not rely on any assumptions, and shows a higher performance and lower error than traditional oxybarometer equations. Feature importance analysis indicates that the machine learning model can well identify fO_2 information in zircon and make fO_2 predictions. The successful application of this oxybarometer to three different geologic situations demonstrates that it has great potential to be widely applicable to geoscience. This work demonstrates that machine learning is a promising tool that can be applied to investigate other regression questions in the Earth sciences.

Data Availability Statement

The datasets, code and software for the machine learning models developed in this study are available at http://doi.org/10.5281/zenodo.7578390 and can be also found at https://github.com/shaohaozou/fO2, which will be updated as more geochemical data of zircon becomes publicly available. Further descriptions regarding the construction of the machine learning models are available through the scikit-learn documentation (https://scikit-learn.org/stable/index.html).

Acknowledgments

This work was co-funded by the National Natural Science Foundation of China (Nos. 42002089, 42102095, 41930428), the Jiangxi Provincial Natural Science Foundation

(Nos. 20224BAB213040, 20224BAB203036, 20224ACB203008), and the DHBK project from East China University of Technology (No. DHBK2019320). We thank two anonymous reviewers and handling editor Claire Bucholz for their very constructive comments, which have markedly improved the quality, presentation and development of the machine learning model described herein. Their suggestions prompted changes that considerably strengthened the work.

References

Abdi, H., and Williams, L.J. (2010) Principal component analysis. Wiley interdisciplinary reviews: computational statistics, 2, 433–459.

Aitchison, J., and Greenacre, M. (2002) Biplots of compositional data. Journal of the Royal Statistical Society: Series C (Applied Statistics), 51, 375–392.

Ballard, J.R., Palin, M.J., and Campbell, I.H. (2002) Relative oxidation states of magmas inferred from Ce(IV)/Ce(III) in zircon: application to porphyry copper deposits of northern Chile. Contributions to Mineralogy and Petrology, 144, 347–364.

Ballhaus, C. (1993) Redox states of lithospheric and asthenospheric upper mantle. Contributions to Mineralogy and Petrology, 114, 331–348.

Bekker, A., Holland, H.D., Wang, P.-L., Rumble, D., Stein, H.J., Hannah, J.L., Coetzee, L.L., and Beukes, N.J. (2004) Dating the rise of atmospheric oxygen. Nature, 427, 117–120.

Breiman, L. (2001) Random forests. Machine learning, 45, 5–32.

Brounce, M.N., Kelley, K.A., and Cottrell, E. (2014) Variations in Fe3+/∑ Fe of Mariana Arc basalts and mantle wedge f O2. Journal of Petrology, 55, 2513–2536.

Bucholz, C., Liebmann, J., and Spencer, C.J. (2022) Secular variability in zircon phosphorus concentrations prevents simple petrogenetic classification. Geochemical Perspectives Letters, 24, 12–16.

Bucholz, C.E. (2022) Coevolution of sedimentary and strongly peraluminous granite

This is the peer-reviewed, final accepted version for American Mineralogist, published by the Mineralogical Society of America.
The published version is subject to change. Cite as Authors (Year) Title. American Mineralogist, in press.
DOI: https://doi.org/10.2138/am-2023-8978. http://www.minsocam.org/

phosphorus records. Earth and Planetary Science Letters, 596, 117795.

Burnham, A.D., and Berry, A.J. (2012) An experimental study of trace element partitioning between zircon and melt as a function of oxygen fugacity. Geochimica et Cosmochimica Acta, 95, 196–212.

Burnham, A.D., and Berry, A.J. (2017) Formation of Hadean granites by melting of igneous crust. Nature Geoscience, 10, 457–461.

Canfield, D.E., Poulton, S.W., and Narbonne, G.M. (2007) Late-Neoproterozoic deep-ocean oxygenation and the rise of animal life. Science, 315, 92–95.

Carmichael, I.S. (1991) The redox states of basic and silicic magmas: a reflection of their source regions? Contributions to Mineralogy and Petrology, 106, 129–141.

Chappell, B.W., and White, A.J.R. (1992) I-and S-type granites in the Lachlan Fold Belt. Earth and Environmental Science Transactions of the Royal Society of Edinburgh, 83, 1–26.

Chen, G., Cheng, Q., Lyons, T.W., Shen, J., Agterberg, F., Huang, N., and Zhao, M. (2022) Reconstructing Earth's atmospheric oxygenation history using machine learning. Nature Communications, 13, 5862.

Chen, H., Su, C., Tang, Y., Li, A., Wu, S., Xia, Q., and ZhangZhou, J. (2021) Machine Learning for Identification of Primary Water Concentrations in Mantle Pyroxene. Geophysical Research Letters, 48.

Chen, T., and Guestrin, C. (2016) Xgboost: A scalable tree boosting system. In Proceedings of the 22nd acm sigkdd international conference on knowledge discovery and data mining pp. 785–794.

Cherniak, D.J., and Watson, E.B. (2003) Diffusion in zircon. Reviews in mineralogy and geochemistry, 53, 113–143.

Christie, D.M., Carmichael, I.S.E., and Langmuir, C.H. (1986) Oxidation states of mid-ocean ridge basalt glasses. Earth and Planetary Science Letters, 79, 397–411.

Cramer, G.M., Ford, R.A., and Hall, R.L. (1976) Estimation of toxic hazard—a decision tree approach. Food and cosmetics toxicology, 16, 255–276.

Crowe, S.A., Døssing, L.N., Beukes, N.J., Bau, M., Kruger, S.J., Frei, R., and Canfield, D.E. (2013) Atmospheric oxygenation three billion years ago. Nature, 501, 535–538.

De Hoog, J.C.M., Lissenberg, C.J., Brooker, R.A., Hinton, R., Trail, D., and Hellebrand, E. (2014) Hydrogen incorporation and charge balance in natural zircon. Geochimica et Cosmochimica Acta, 141, 472–486.

Evans, K.A., Elburg, M.A., and Kamenetsky, V.S. (2012) Oxidation state of subarc mantle. Geology, 40, 783–786.

Ferry, J.M., and Watson, E.B. (2007) New thermodynamic models and revised calibrations for the Ti-in-zircon and Zr-in-rutile thermometers. Contributions to Mineralogy and Petrology, 154, 429–437.

Frei, R., Gaucher, C., Poulton, S.W., and Canfield, D.E. (2009) Fluctuations in Precambrian atmospheric oxygenation recorded by chromium isotopes. Nature, 461, 250–253.

Fukunaga, K., and Narendra, P.M. (1975) A branch and bound algorithm for computing k-nearest neighbors. IEEE transactions on computers, 100, 750–753.

Geurts, P., Ernst, D., and Wehenkel, L. (2006) Extremely randomized trees. Machine learning, 63, 3–42.

Ghiorso, M.S., and Evans, B.W. (2008) Thermodynamics of rhombohedral oxide solid solutions and a revision of the Fe-Ti two-oxide geothermometer and oxygen-barometer. American Journal of science, 308, 957–1039.

Hall, M.A. (1999) Correlation-based feature selection for machine learning. PhD Thesis, The University of Waikato.

Higgins, O., Sheldrake, T., and Caricchi, L. (2022) Machine learning thermobarometry and chemometry using amphibole and clinopyroxene: a window into the roots of an arc volcano (Mount Liamuiga, Saint Kitts). Contributions to Mineralogy and Petrology, 177, 10.

Hodgskiss, M.S.W., and Sperling, E.A. (2022) A prolonged, two-step oxygenation of Earth's early atmosphere: Support from confidence intervals. Geology, 50, 158–162.

Hoskin, P.W.O., and Schaltegger, U. (2003) The composition of zircon and igneous and metamorphic petrogenesis. Reviews in mineralogy and geochemistry, 53, 27–62.

Huang, W., Lyu, Y., Du, M., He, C., Gao, S., and Xu, R. (2022) Estimating ferric iron content in clinopyroxene using machine learning models. American Mineralogist, 48.

Jackson, J.E. (2005) A user's guide to principal components, 1–597 p. John Wiley & Sons.

Jorgenson, C., Higgins, O., Petrelli, M., Bégué, F., and Caricchi, L. (2022) A Machine Learning-Based Approach to Clinopyroxene Thermobarometry: Model Optimization and Distribution for Use in Earth Sciences. Journal of Geophysical Research: Solid Earth, 127, e2021JB022904.

Jugo, P.J., Wilke, M., and Botcharnikov, R.E. (2010) Sulfur K-edge XANES analysis of natural and synthetic basaltic glasses: Implications for S speciation and S content as function of oxygen fugacity. Geochimica et Cosmochimica Acta, 74, 5926–5938.

Kaufman, A.J., Johnston, D.T., Farquhar, J., Masterson, A.L., Lyons, T.W., Bates, S., Anbar, A.D., Arnold, G.L., Garvin, J., and Buick, R. (2007) Late Archean Biospheric Oxygenation and Atmospheric Evolution. Science, 317, 1900–1903.

Keller, C.B., and Schoene, B. (2012) Statistical geochemistry reveals disruption in secular lithospheric evolution about 2.5 Gyr ago. Nature, 485, 490–493.

Kirkland, C.L., Smithies, R.H., Taylor, R.J.M., Evans, N., and McDonald, B. (2015) Zircon Th/U ratios in magmatic environs. Lithos, 212, 397–414.

Kress, V.C., and Carmichael, I.S.E. (1991) The compressibility of silicate liquids containing Fe2O3 and the effect of composition, temperature, oxygen fugacity and pressure on their redox states. Contributions to Mineralogy and Petrology, 108, 82–92.

Lee, C.-T.A., and Bachmann, O. (2014) How important is the role of crystal fractionation in making intermediate magmas? Insights from Zr and P systematics. Earth and Planetary Science Letters, 393, 266–274.

Lee, C.-T.A., Luffi, P., Le Roux, V., Dasgupta, R., Albaréde, F., and Leeman, W.P. (2010) The redox state of arc mantle using Zn/Fe systematics. Nature, 468, 681–685.

Li, X., and Zhang, C. (2022) Machine Learning Thermobarometry for Biotite-Bearing Magmas. Journal of Geophysical Research: Solid Earth, 127.

Lin, X., Cicchella, D., Hong, J., and Meng, G. (2022) A Test of the Hypothesis That Syn-Collisional Felsic Magmatism Contributes to Continental Crustal Growth Via Deep Learning Modeling and Principal Component Analysis of Big Geochemical Datasets. Journal of Geophysical Research: Solid Earth, 127.

Liu, H., Zartman, R.E., Ireland, T.R., and Sun, W. (2019) Global atmospheric oxygen variations recorded by Th/U systematics of igneous rocks. Proceedings of the National Academy of Sciences, 116, 18854–18859.

Liu, X.-M., Kah, L.C., Knoll, A.H., Cui, H., Wang, C., Bekker, A., and Hazen, R.M. (2021) A persistently low level of atmospheric oxygen in Earth's middle age. Nature Communications, 12, 351.

Loader, M.A., Wilkinson, J.J., and Armstrong, R.N. (2017) The effect of titanite crystallisation on Eu and Ce anomalies in zircon and its implications for the assessment of porphyry Cu deposit fertility. Earth and Planetary Science Letters, 472, 107–119.

Lösing, M., and Ebbing, J. (2021) Predicting Geothermal Heat Flow in Antarctica With a Machine Learning Approach. Journal of Geophysical Research: Solid Earth, 126.

Loucks, R.R., Fiorentini, M.L., and Rohrlach, B.D. (2018) Divergent T–fO_2 paths during crystallisation of H_2O-rich and H_2O-poor magmas as recorded by Ce and U in zircon, with implications for TitaniQ and TitaniZ geothermometry. Contributions to Mineralogy and Petrology, 173, 104.

Loucks, R.R., Fiorentini, M.L., and Henríquez, G.J. (2020) New Magmatic Oxybarometer Using Trace Elements in Zircon. Journal of Petrology, 61, egaa034.

Lu, Y., Loucks, R., Fiorentini, M., McCuaig, T., Evans, N.J., Yang, Z.-M., Hou, Z.-Q., Kirkland, C.L., Avila, L.P., and Kobussen, A. (2016) Zircon compositions as a pathfinder for porphyry Cu±Mo±Au deposits. Society of Economic Geologists. Special Publications Series, 19, 329–347.

Lundberg, S.M., and Lee, S.-I. (2017) A unified approach to interpreting model predictions. In Proceedings of the 31st international conference on neural information processing systems pp. 4768–4777.

Lyons, T.W., Reinhard, C.T., and Planavsky, N.J. (2014) The rise of oxygen in Earth's early ocean and atmosphere. Nature, 506, 307–315.

Meng, X., Kleinsasser, J.M., Richards, J.P., Tapster, S.R., Jugo, P.J., Simon, A.C., Kontak, D.J., Robb, L., Bybee, G.M., Marsh, J.H., and others (2021) Oxidized sulfur-rich arc magmas formed porphyry Cu deposits by 1.88 Ga. Nature Communications, 12, 2189.

Nathwani, C.L., Wilkinson, J.J., Fry, G., Armstrong, R.N., Smith, D.J., and Ihlenfeld, C. (2022) Machine learning for geochemical exploration: classifying metallogenic fertility in arc magmas and insights into porphyry copper deposit formation. Mineralium Deposita.

Ni, Z., Arevalo, R., Piccoli, P., and Reno, B.L. (2020) A Novel Approach to Identifying Mantle-Equilibrated Zircon by Using Trace Element Chemistry. Geochemistry, Geophysics, Geosystems, 21.

Partin, C.A., Bekker, A., Planavsky, N.J., Scott, C.T., Gill, B.C., Li, C., Podkovyrov, V., Maslov, A., Konhauser, K.O., Lalonde, S.V., and others (2013) Large-scale fluctuations in Precambrian atmospheric and oceanic oxygen levels from the record of U in shales. Earth and Planetary Science Letters, 369–370, 284–293.

Petrelli, M., and Perugini, D. (2016) Solving petrological problems through machine learning: the study case of tectonic discrimination using geochemical and isotopic data. Contributions to Mineralogy and Petrology, 171, 81.

Petrelli, M., Caricchi, L., and Perugini, D. (2020) Machine Learning Thermo-Barometry: Application to Clinopyroxene-Bearing Magmas. Journal of Geophysical Research: Solid Earth, 125.

Planavsky, N.J., Asael, D., Hofmann, A., Reinhard, C.T., Lalonde, S.V., Knudsen, A., Wang, X., Ossa Ossa, F., Pecoits, E., Smith, A.J.B., and others (2014) Evidence for oxygenic photosynthesis half a billion years before the Great Oxidation Event. Nature Geoscience, 7, 283–286.

Qin, B., Huang, F., Huang, S., Python, A., Chen, Y., and ZhangZhou, J. (2022) Machine Learning Investigation of Clinopyroxene Compositions to Evaluate and Predict Mantle Metasomatism Worldwide. Journal of Geophysical Research: Solid Earth, 127.

Reinhard, C.T., and Planavsky, N.J. (2022) The History of Ocean Oxygenation. Annual Review of Marine Science, 14, 331–353.

Rezeau, H., and Jagoutz, O. (2020) The importance of H2O in arc magmas for the formation of porphyry Cu deposits. Ore Geology Reviews, 126, 103744.

Richards, J.P. (2015) The oxidation state, and sulfur and Cu contents of arc magmas: implications for metallogeny. Lithos, 233, 27–45.

Ridolfi, F. (2021) Amp-TB2: An Updated Model for Calcic Amphibole Thermobarometry. Minerals, 11, 324.

Ridolfi, F., and Renzulli, A. (2012) Calcic amphiboles in calc-alkaline and alkaline magmas: thermobarometric and chemometric empirical equations valid up to 1,130°C and 2.2 GPa. Contributions to Mineralogy and Petrology, 163, 877–

895.

Rutherford, M.J., and Hill, P.M. (1993) Magma ascent rates from amphibole breakdown: an experimental study applied to the 1980–1986 Mount St. Helens eruptions. Journal of Geophysical Research: Solid Earth, 98, 19667–19685.

Scott, C., Lyons, T.W., Bekker, A., Shen, Y., Poulton, S.W., Chu, X., and Anbar, A.D. (2008) Tracing the stepwise oxygenation of the Proterozoic ocean. Nature, 452, 456–459.

Shen, P., Hattori, K., Pan, H., Jackson, S., and Seitmuratova, E. (2015) Oxidation condition and metal fertility of granitic magmas: Zircon trace-element data from porphyry Cu deposits in the Central Asian orogenic belt. Economic Geology, 110, 1861–1878.

Sillitoe, R.H. (2010) Porphyry Copper Systems. Economic Geology, 105, 3–41.

Smola, A.J., and Schölkopf, B. (2004) A tutorial on support vector regression. Statistics and computing, 14, 199–222.

Smythe, D.J., and Brenan, J.M. (2016) Magmatic oxygen fugacity estimated using zircon-melt partitioning of cerium. Earth and Planetary Science Letters, 453, 260–266.

Streck, M.J., and Dilles, J.H. (1998) Sulfur evolution of oxidized arc magmas as recorded in apatite from a porphyry copper batholith. Geology, 26, 523–526.

Sun, W., Huang, R., Li, H., Hu, Y., Zhang, C., Sun, S., Zhang, L., Ding, X., Li, C., Zartman, R.E., and others (2015) Porphyry deposits and oxidized magmas. Ore Geology Reviews, 65, 97–131.

Tang, M., Chu, X., Hao, J., and Shen, B. (2021) Orogenic quiescence in Earth's middle age. Science, 371, 728–731.

Trail, D., Thomas, J.B., and Watson, E.B. (2011a) The incorporation of hydroxyl into zircon. American Mineralogist, 96, 60–67.

Trail, D., Watson, E.B., and Tailby, N.D. (2011b) The oxidation state of Hadean magmas and implications for early Earth's atmosphere. Nature, 480, 79–82.

van den Boogaart, K.G., and Tolosana-Delgado, R. (2013) Analyzing compositional data with R Vol. 122. Springer.

Wang, J., Xiong, X., Takahashi, E., Zhang, L., Li, L., and Liu, X. (2019) Oxidation State of Arc Mantle Revealed by Partitioning of V, Sc, and Ti Between Mantle Minerals and Basaltic Melts. Journal of Geophysical Research: Solid Earth, 124, 4617–4638.

Wang, L., Su, C., Wang, L.-Q., ZhangZhou, J., Xia, Q.-K., and Wang, Q.-Y. (2022) Refined estimation of Li in mica by a machine learning method. American Mineralogist, 107, 1034–1044.

Zhang, H.L., Cottrell, E., Solheid, P.A., Kelley, K.A., and Hirschmann, M.M. (2018) Determination of Fe3+/ΣFe of XANES basaltic glass standards by Mössbauer spectroscopy and its application to the oxidation state of iron in MORB. Chemical Geology, 479, 166–175.

Zhong, S., Seltmann, R., Qu, H., and Song, Y. (2019) Characterization of the zircon Ce anomaly for estimation of oxidation state of magmas: a revised Ce/Ce* method. Mineralogy and Petrology, 113, 755–763.

Zhong, S.H., Liu, Y., Li, S.Z., Bindeman, I.N., Cawood, P.A., Seltmann, R., Niu, J.H., Guo, G.H., and Liu, J.Q. (2023) A machine learning method for distinguishing detrital zircon provenance. Contributions to Mineralogy and Petrology, 178, 35.

Zhu, Z., Campbell, I.H., Allen, C.M., and Burnham, A.D. (2020) S-type granites: Their origin and distribution through time as determined from detrital zircons. Earth and Planetary Science Letters, 536, 116140.

Zou, S., Chen, X., Xu, D., Brzozowski, M.J., Lai, F., Bian, Y., Wang, Z., and Deng, T. (2021) A machine learning approach to tracking crustal thickness variations in the eastern North China Craton. Geoscience Frontiers, 12, 101195.

Zou, S., Chen, X., Brzozowski, M.J., Leng, C., and Xu, D. (2022) Application of machine learning to characterizing magma fertility in porphyry Cu deposits. Journal of Geophysical Research: Solid Earth, 127, 2022JB024584.

Zou, X., Qin, K., Han, X., Li, G., Evans, N.J., Li, Z., and Yang, W. (2019) Insight into zircon REE oxy-barometers: A lattice strain model perspective. Earth and Planetary Science Letters, 506, 87–96.

Figure captions

Figure 1. Schematic diagram illustrating the data pre-processing and construction workflow used for the development of machine learning models.

Figure 2. Compositional biplots for a) PC1–PC2 and b) PC2–PC3 showing the zircon data points and principle component loadings. PC loadings for each element are plotted as orange lines. The numbers in brackets in the axis titles denote the variance accounted for by the PCs. (c) Scree plot for zircon trace-element chemistry combined with the cumulative explanation of the total variance of PCs.

Figure 3. Probability density distribution of (a) R^2 and (b) RMSE values for predictions made on the test dataset by the machine learning algorithms. The values are based on 1000 Monte Carlo simulations.

Figure 4. Results of the propagated error calculated based on the trace-element contents of zircon obtained via 1000 Monte Carlo simulations. (a) The fO_2 values predicted using the machine learning-based oxybarometer, and (b) the probability density distribution and kernel density estimation for residuals (from machine learning-based oxybarometer) between the predicted and the measured fO_2 values. (c) The fO_2 values calculated using the U–Ti–Ce equation, and (d) the probability density

distribution and kernel density estimation for residuals (from U–Ti–Ce equation) between the calculated and measured fO_2 values.

Figure 5. (a) Feature importance bar plots generated by the extremely randomized trees algorithm, which shows the relative importance of different elements when predicting the fO_2 value of a magma. (b) SHAP summary plots showing the influence of individual samples on the prediction. The SHAP value of the individual elements are calculated across all samples, which are used to explore the impact of each element on predicting the fO_2 values. The color of the data point (from red to blue) illustrates the influence of a feature on the output of the prediction value (from high to low).

Figure 6. Box-whisker plots illustrating the range of fO_2 values of arcs and MORBs predicted by the machine learning-based oxybarometer. The original data are collated from the GEOROC database and the utilized data (after filtering) are provided in Table S4.

Figure 7. Box-whisker plots illustrating the range of fO_2 values of fertile and barren rocks from porphyry systems using the machine learning-based oxybarometer.

Figure 8. (a) The fO_2 values are predicted using our machine learning-based oxybarometer and zircons from S-type granites. (b) Sediments U contents in black shales (Scott et al. 2008). (c) The blue line shows the best estimate of atmospheric

oxygen (pO_2 (% PAL)) best on the Ce anomaly in marine carbonates (in red line), which are from Liu et al. (2021).

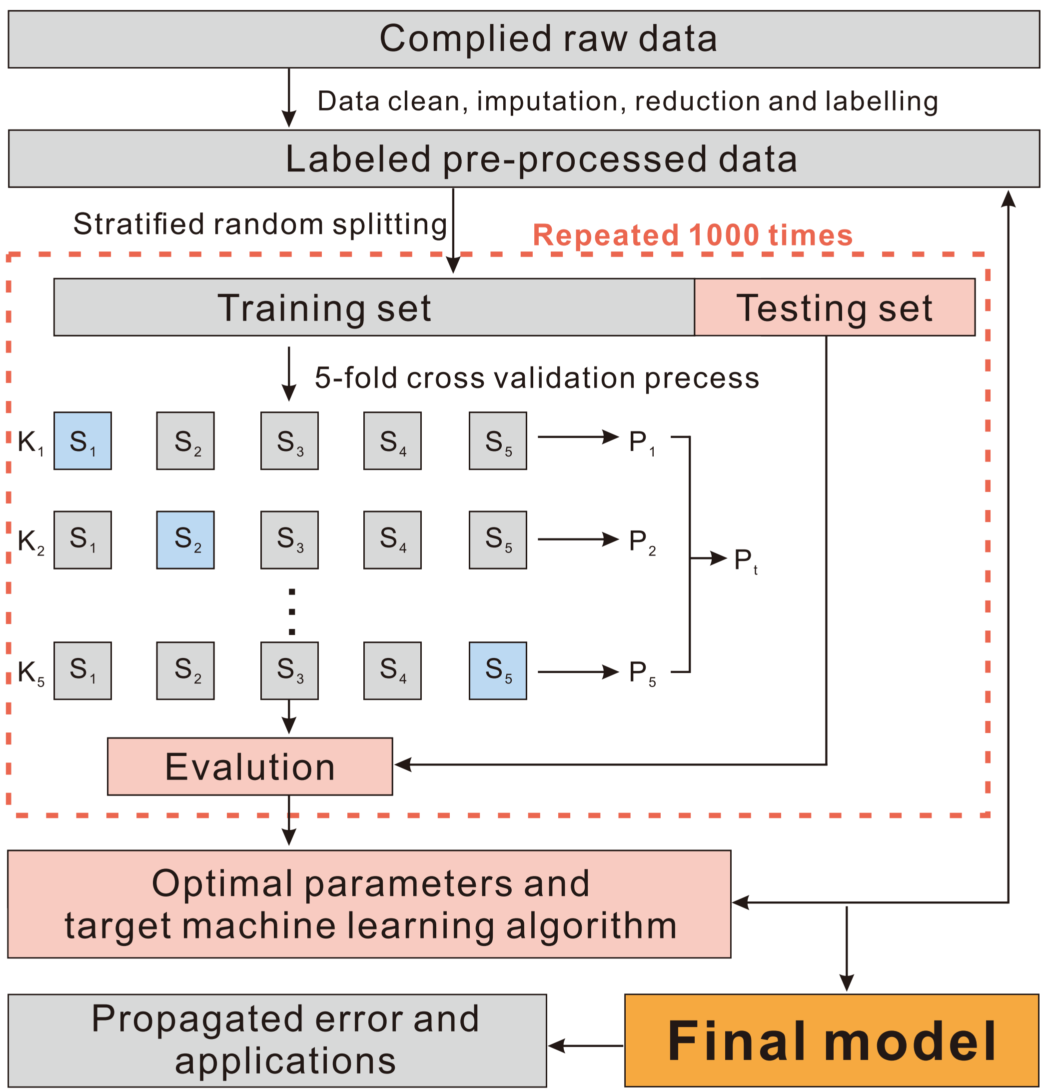
Complied raw data
Data clean, imputation, reduction and labelling
Labeled pre-processed data
Stratified random splitting
Repeated 1000 times
Training set
Testing set
5-fold cross validation precess
K1 S1 S2 S3 S4 S5 P1
K2 S1 S2 S3 S4 S5 P2
Pt
K5 S1 S2 S3 S4 S5 P5
Evalution
Optimal parameters and target machine learning algorithm
Propagated error and applications
Final model

Figure 1

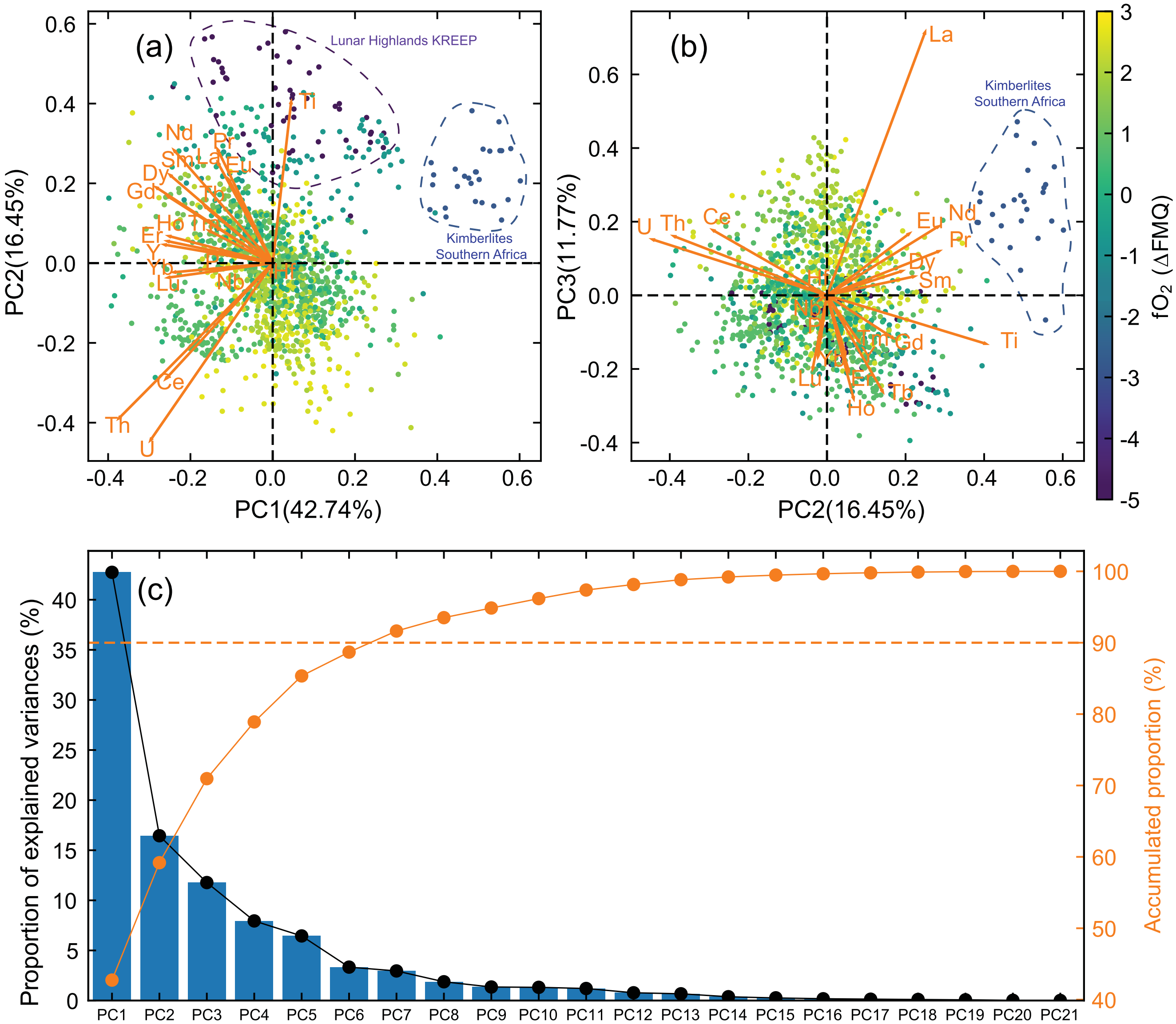
(a)
Lunar Highlands KREEP
Kimberlites
Southern Africa
PC1(42.74%)
PC2(16.45%)
Ti
Nd
Pr
Sm
La
Eu
Dy
Gd
Ho
Er
Y
Yb
Lu
Nb
Ce
Th
U
(b)
La
Kimberlites
Southern Africa
U
Th
Ce
Eu
Nd
Pr
Dy
Sm
Ti
Gd
Lu
Ho
PC2(16.45%)
PC3(11.77%)
fO2 (ΔFMQ)
(c)
Proportion of explained variances (%)
Accumulated proportion (%)
PC1
PC2
PC3
PC4
PC5
PC6
PC7
PC8
PC9
PC10
PC11
PC12
PC13
PC14
PC15
PC16
PC17
PC18
PC19
PC20
PC21

Figure 2

This is the peer-reviewed, final accepted version for American Mineralogist, published by the Mineralogical Society of America.
The published version is subject to change. Cite as Authors (Year) Title. American Mineralogist, in press.
DOI: https://doi.org/10.2138/am-2023-8978. http://www.minsocam.org/

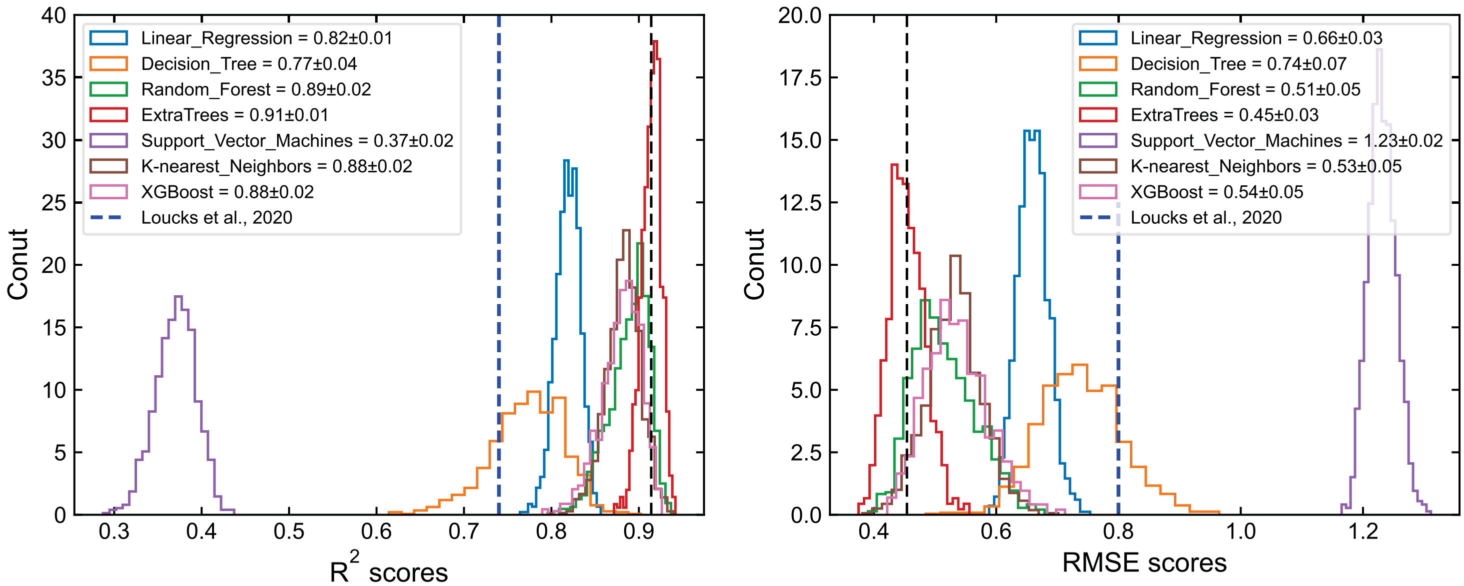

Figure 3

This is the peer-reviewed, final accepted version for American Mineralogist, published by the Mineralogical Society of America.
The published version is subject to change. Cite as Authors (Year) Title. American Mineralogist, in press.
DOI: https://doi.org/10.2138/am-2023-8978. http://www.minsocam.org/

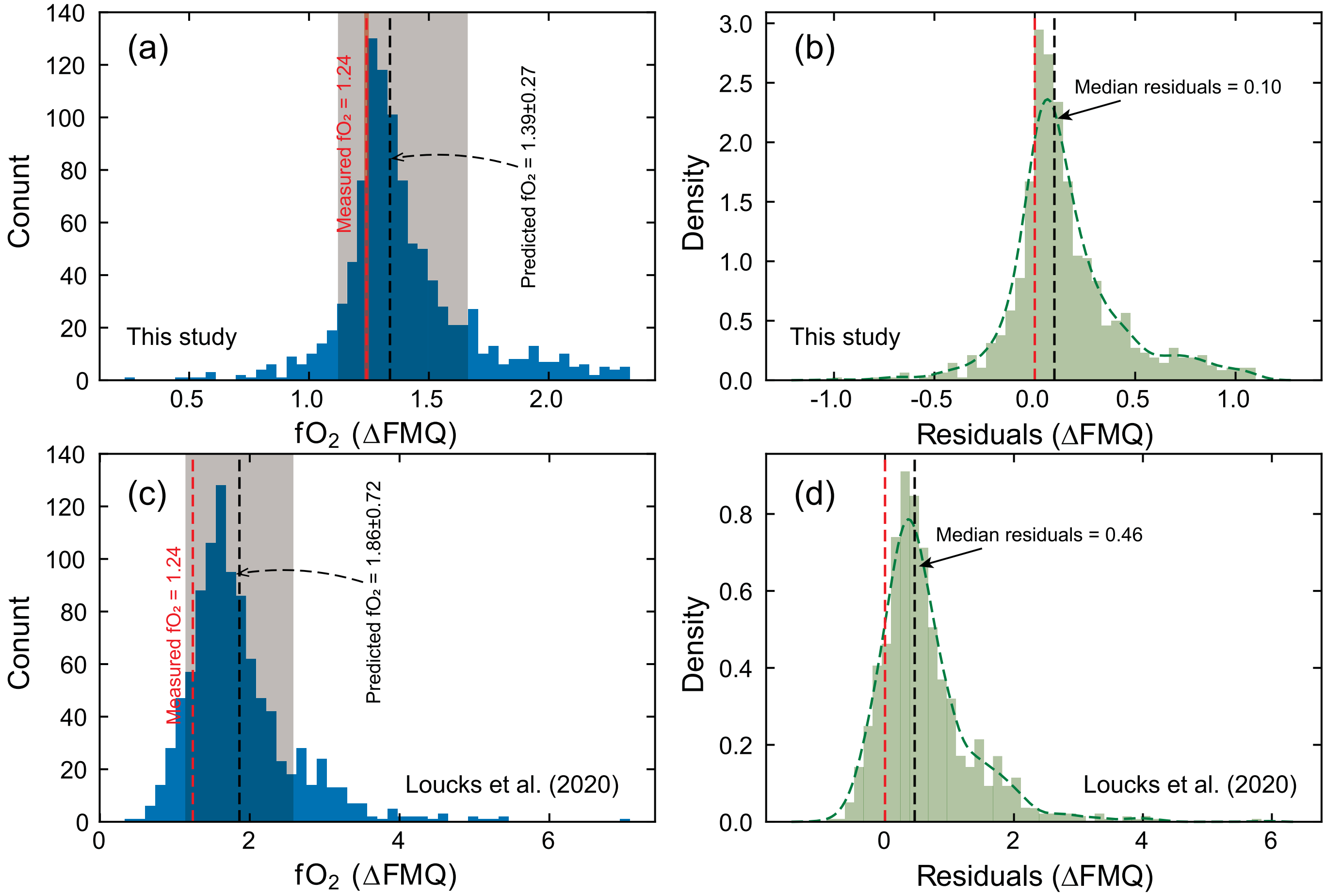

Figure 4

This is the peer-reviewed, final accepted version for American Mineralogist, published by the Mineralogical Society of America.
The published version is subject to change. Cite as Authors (Year) Title. American Mineralogist, in press.
DOI: https://doi.org/10.2138/am-2023-8978. http://www.minsocam.org/

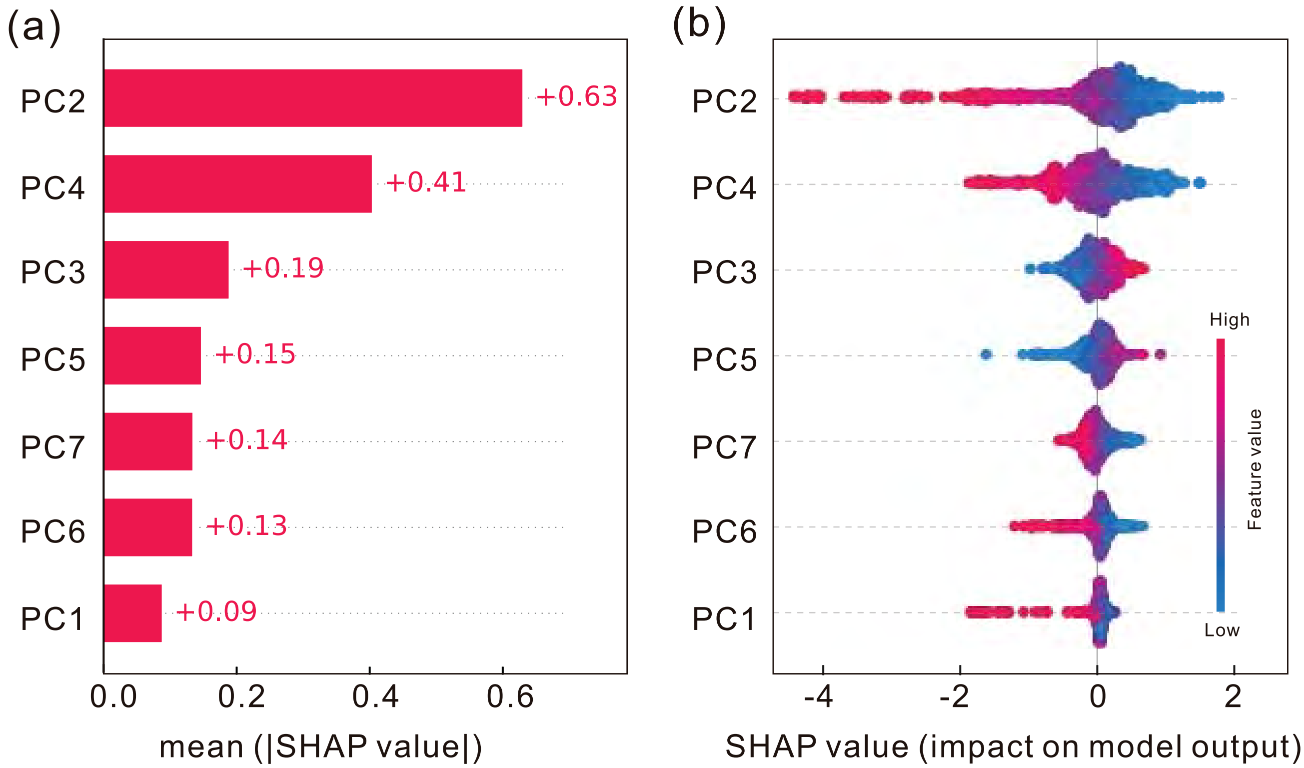

Figure 5

This is the peer-reviewed, final accepted version for American Mineralogist, published by the Mineralogical Society of America.
The published version is subject to change. Cite as Authors (Year) Title. American Mineralogist, in press.
DOI: https://doi.org/10.2138/am-2023-8978. http://www.minsocam.org/

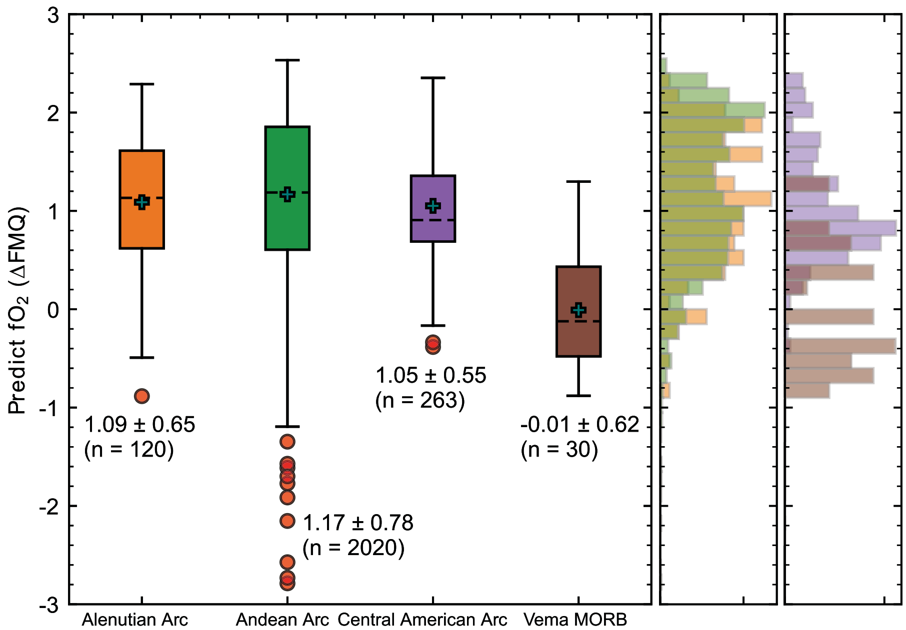

Figure 6

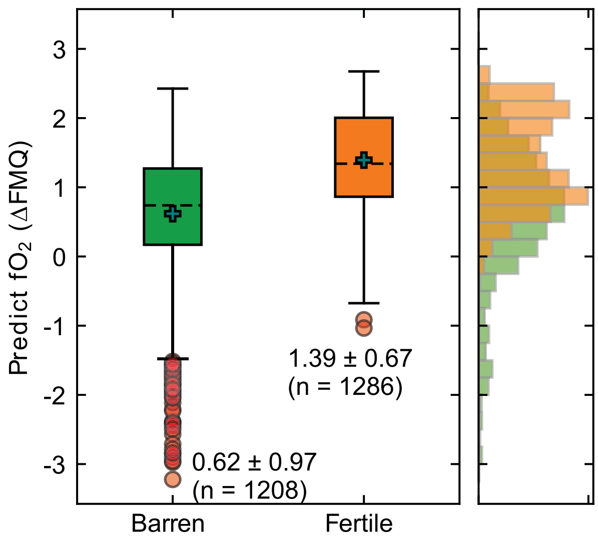
3
2
1
0
-1
-2
-3
Predict fO2 (ΔFMQ)
1.39 ± 0.67
(n = 1286)
0.62 ± 0.97
(n = 1208)
Barren
Fertile

Figure 7

This is the peer-reviewed, final accepted version for American Mineralogist, published by the Mineralogical Society of America.
The published version is subject to change. Cite as Authors (Year) Title. American Mineralogist, in press.
DOI: https://doi.org/10.2138/am-2023-8978. http://www.minsocam.org/

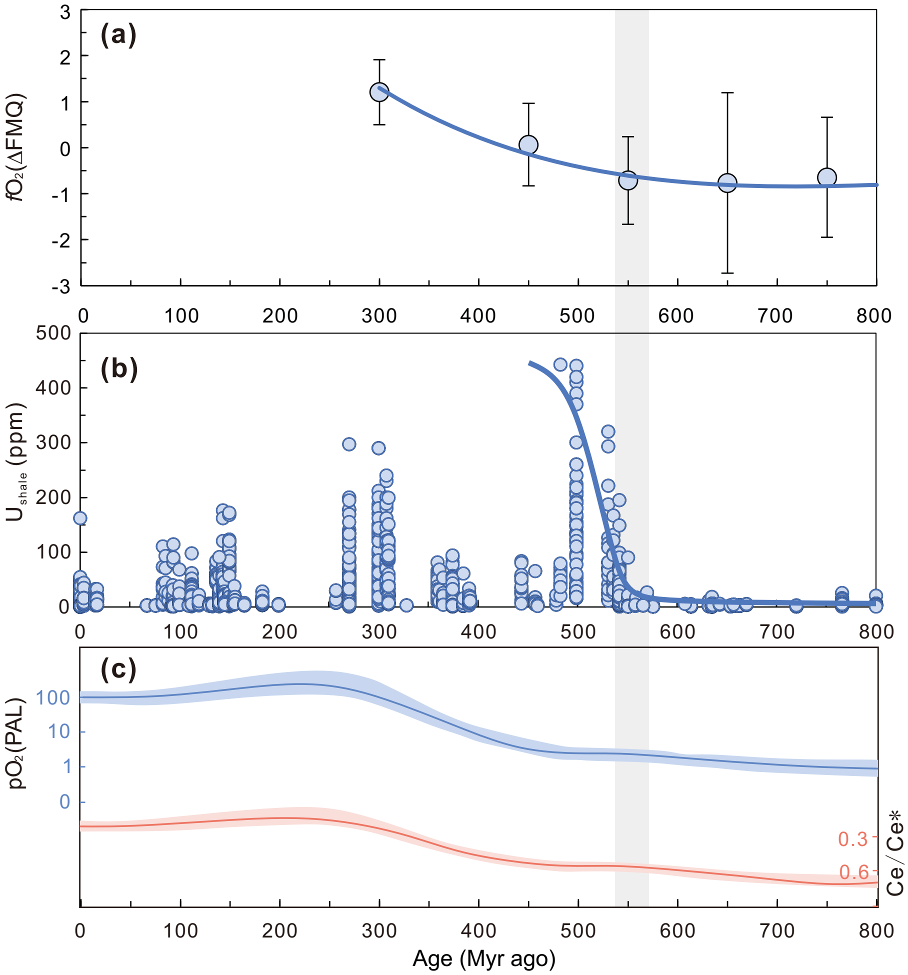

Figure 8